Projecting dry-wet abrupt alternation across China from the perspective of soil moisture

Jianxiu Qiu, Chenxi He, Xiaoping Liu, Lun Gao, Chao Tan, Xinghan Wang, Dongdong Kong, Wigneron J.-P., Deliang Chen, Jun Xia

HAL Id: hal-04779501
https://hal.inrae.fr/hal-04779501v1

Submitted on 13 Nov 2024

Projecting dry-wet abrupt alternation across China from the perspective of soil moisture

Check for updates

Jianxiu Qiu [1,2] ✉**, Chenxi He** [1]**, Xiaoping Liu**[1]**, Lun Gao**[3]**, Chao Tan**[4]**, Xinghan Wang**[5]**, Dongdong Kong**[6]**, Jean-Pierre Wigneron**[7]**, Deliang Chen** [8,9] **& Jun Xia**[10]

Under a warmer climate, the enhancement of dry-wet abrupt alternation (DWAA) risk poses a great challenge for sustainable development. Here, we introduce a novel framework for DWAA detection based on our proposed soil moisture concentration index. By the end of this century, over humid southern China, the shift of soil moisture time series from anomalously wet to anomalously dry pattern, or the other way around, will be more abrupt. In addition, the proposed framework driven by Coupled Model Intercomparison Project Phase 6 simulations projects more widespread DWAA-affected areas over southwestern China, coastal regions of southeastern China, and the lower reaches of the Yangtze River, especially under a high emission scenario. The framework proposed in this study provides an efficient system for DWAA detection and prediction, and the findings of this study provide a reference for upgrading hydraulic infrastructure and mitigating future DWAA events.

Under a global warming scenario, extreme events, such as heavy rainfall, flooding, and drought, are likely to increase in frequency globally[1–3]. Among these events, abrupt switches between the two extreme states of drought and flood, namely dry-wet abrupt alternation (DWAA), exert far more severe socioeconomic impacts than a single drought or flood event[4–6]. A DWAA event covers both ends of the spectrum including wet-to-dry (WD) state, dry-to-wet (DW) state and the rapid switch between these two extreme states[7,8]. Such events can cause geological disasters[9,10], ecological stress[11,12], and severe conflict between domestic water supply and demand[13,14]. However, the lack of adequate methods for quantifying DWAA deeply constrained our insight into the changing DWAA pattern in the coming decades.

Conventionally, DWAA events were identified using a univariate rainfall[15] or runoff[16,17], or multivariate composite indices, such as the standardized precipitation evapotranspiration index (SPEI)[18] or Palmer drought severity index (PDSI)[19]. Among these, the univariate rainfall or runoff can indicate a rapid switch from dry to wet state for one single end of the DWAA spectrum, whereas it cannot characterize abrupt alternation from wet to dry state at the other end of the spectrum (such as flash droughts), as it does not contain direct information on water demand such as evapotranspiration. The metric of precipitation−evapotranspiration ($P-E$) has proved to be generally well-fitted for evaluating the changes in water availability over the ocean. However, $P-E$ shows a large inter-model spread due to substantial disagreement in both P and E projections by different global climate models (GCMs)[20–22]. In addition, multivariate drought indices require parametric fitting and are thus unsuitable for tracking non-stationary hydrometeorological conditions under a changing climate. Moreover, previous DWAA research was largely conducted at a monthly timescale, which is suitable for recording conventional meteorological droughts (e.g., using one- or three-month SPEI), whereas it cannot effectively capture the rapid evolution of DWAA events, seriously reducing the forecast lead time of DWAA.

The key to the efficient detection of DWAA events is the accurate measurement of seasonality or temporal concentration of soil water availability. Compared with the above-mentioned metrics, daily-scale soil moisture (SM), as an integrator of rainfall, evapotranspiration (ET) and

[1]Guangdong Provincial Key Laboratory of Urbanization and Geo-simulation, School of Geography and Planning, Sun Yat-sen University, Guangzhou, 510275, China. [2]Key Innovative Research Team of Liaoning Provincial Meteorological Bureau, Shenyang, 110166, China. [3]Institute on the Environment, University of Minnesota, St. Paul, MN, 55108, USA. [4]Guangdong Research Institute of Water Resources and Hydropower, Guangzhou, 510630, China. [5]Water Resources Remote Sensing Department, Pearl River Water Resources Research Institute, Guangzhou, 510610, China. [6]Department of Atmospheric Science, School of Environmental Studies, China University of Geosciences, Wuhan, 430078, China. [7]INRAE, UMR1391 ISPA, Universit´e de Bordeaux, Bordeaux, Villenave d'Ornon, 33140, France. [8]Department of Earth System Sciences, Tsinghua University, Beijing, 100084, China. [9]Department of Earth Sciences, University of Gothenburg, Gothenburg, 40530, Sweden. [10]State Key Laboratory of Water Resources Engineering and Management, Wuhan University, Wuhan, 430072, China. ✉e-mail: qiujianxiu@mail.sysu.edu.cn

runoff, is more directly relevant to terrestrial ecosystem[23], and can therefore accurately quantify the ecological impact of a given DWAA event. In addition, surface SM can depict a rapid occurrence of either WD or DW event, as opposed to precipitation, which cannot characterize a rapid wet-to-dry switch since rainless for a short period does not necessarily indicate drought. Moreover, the daily scale of the surface SM dataset is more appropriate for detecting the rapid change of terrestrial water status, compared to the monthly drought index such as SPEI.

In this study, we propose a novel metric, namely the soil moisture concentration index (SMCI), for measuring the seasonality of soil water resources. The SMCI is proposed based on the Gini index, an economic concept that expresses the degree of inequality in terms of the difference between the curve of real income distribution (known as the Lorenz curve or the concentration curve) and the curve of absolute equality of income distribution. The closer the Gini index to zero, the more equal the income distribution tends to be. Recently, similar concept of Gini index has been applied in the field of hydrometeorology, such as characterizing the concentration of precipitation[24–26].

In this study, such a concept is innovatively applied to SM in a modified way. That is, without the sorting operations on the SM time series, the cumulative curve of the raw SM time series within a time window and the cumulative curve of the assumed uniformly distributed SM time series are plotted separately, so that the cumulative difference between the two curves can be either positive or negative, which corresponds to SM shift from wetter (relative to the SM average of the time window considered) end to drier end, or vice versa. This cumulative difference is further normalized by the cumulation of the assumed uniformly distributed SM time series, and denoted as SMCI.

Further, based on the distribution theory of runs[27], this proposed SMCI is used in combination with soil moisture anomaly (SMA) to construct an effective framework for DWAA detection (more details in Methods). We use this framework to investigate the historical and future projection of DWAA spatiotemporal patterns over China, which is sensitive to drought and flood disasters due to complex topography and monsoonal climate, especially under climate change[28–30]. Finally, we attribute the SMCI pattern to the critical hydrometeorological variables, including rainfall, ET, and runoff, all of which expressed in concentration indices, and thus identify the main factor dominating SMCI and potential DWAA over different climatic regions of China.

Results

Spatial distribution of SMCI over China

The positive or negative signs of SMCI indicate potential occurrences of either WD or DW event, and the magnitude of SMCI (|SMCI|) measures the abruptness degree of SM time series shift from anomalously wet pattern to anomalously dry pattern, or the other way around. In addition, without the sorting operation, the corresponding SMCI is defined for each time point within a sliding window, which makes SMCI a more dynamic index.

For the growing season (April to September) of 1979–2100, the median of SMCI (Fig. 1a) and absolute SMCI (|SMCI|; Fig. 1b) are estimated based on the surface SM simulations from multi-model ensemble mean (MME) of Coupled Model Intercomparison Project Phase 6 (CMIP6) under the SSP2-4.5 scenario (more details in Methods). In SSP2-4.5, "SSP2" represents conditions under shared socioeconomic pathway 2, "4.5" indicates an additional radiative forcing of 4.5 W/m² in the year 2100 based on a medium forcing (or "business-as-usual") scenario. It shows that the temporal concentration of SM is highest over the semi-arid to arid region (AR) in northwestern China. It is followed by the transition region (TR) which transitions from arid to humid region (HR). The lowest SMCI occurs in the adjacent region between HR and plateau climate region (PR), indicating comparatively uniform temporal distribution in this region.

A similar pattern is observed in Fig. 1a, b, except that negative SMCI is prevalent in the eastern PR and western HR (Fig. 1a). As indicated in Methods, SMCI is superior to the conventional precipitation concentration index (PCI)[31], in that SMCI differentiates temporal concentration by its positive and negative signs. In case of negative SMCI, the cumulative curve of actual SM is initially more flatten than hypothetical uniformly distributed SM, and then grows steeper than the latter, demonstrating a concave shape in actual SM time series cumulative curve. This indicates that SM is initially lower than the average within the time window, or at the dry end of the time window considered, and then switches to the wetter end. The abruptness of the switch can be inferred from the difference in curvatures of two cumulative curve sections, or the area integrated by the cumulative curve of actual SM minus the hypothetical uniformly distributed SM. On the other hand, the positive SMCI, or convexity of the cumulative curve, indicates otherwise. Therefore, the eastern PR and western HR show a higher probability of DW event occurrence. This trend has already been observed over PR where rainy days are more prevalent within the course of a year due to increasing water vapor source[32].

In addition, the discrepancy of SMCI between EC-Earth3 and EC-Earth3-Veg emphasizes the role played by vegetation in smoothing out the temporal unevenness of SM in western arid China, where the shift of SM time series from anomalously wet to anomalously dry pattern, or the other way around is very abrupt (Supplementary Note 1). Furthermore, this study shows high spatial consistency and temporal correlation between |SMCI| generated using three extensively-used SM datasets, namely CMIP6, the fifth generation reanalysis from European Centre for Medium-Range Weather Forecasts (ERA5), and product from Soil Moisture Active Passive mission (SMAP) (Supplementary Note 2).

Temporal trend of SMCI

The temporal trend of the annual mean |SMCI| is analyzed using the Theil–Sen estimator, and the normalized regression slope (i.e., grid-based slope divided by grid-based annual mean |SMCI|) is shown in Fig. 2. Under the median CO_2 emission level (SSP2-4.5 scenario), the increasing trend of SMCI is most prominent, with significance level of $p < 0.05$ across most of HR, and with highest increasing magnitude over southwestern HR during the entire study period 1979–2100. This indicates increasing potential for

Fig. 1 | Spatial distribution of SMCI based on surface SM simulations of CMIP6 MME for 1979–2100 under the SSP2-4.5 scenario. a The median of SMCI, **b** the median of |SMCI|. The inset violin plots at the bottom left of each sub-figure show the spread of SMCI or |SMCI| for each sub-region, with the horizontal dashed lines indicating 25th, 50th, and 75th percentiles from bottom to top. Sub-region classification is based on a climatic zoning map compiled by the China Meteorological Administration.
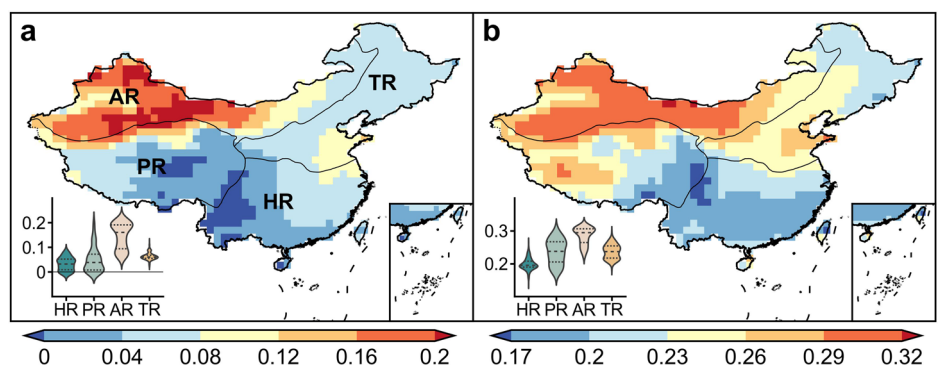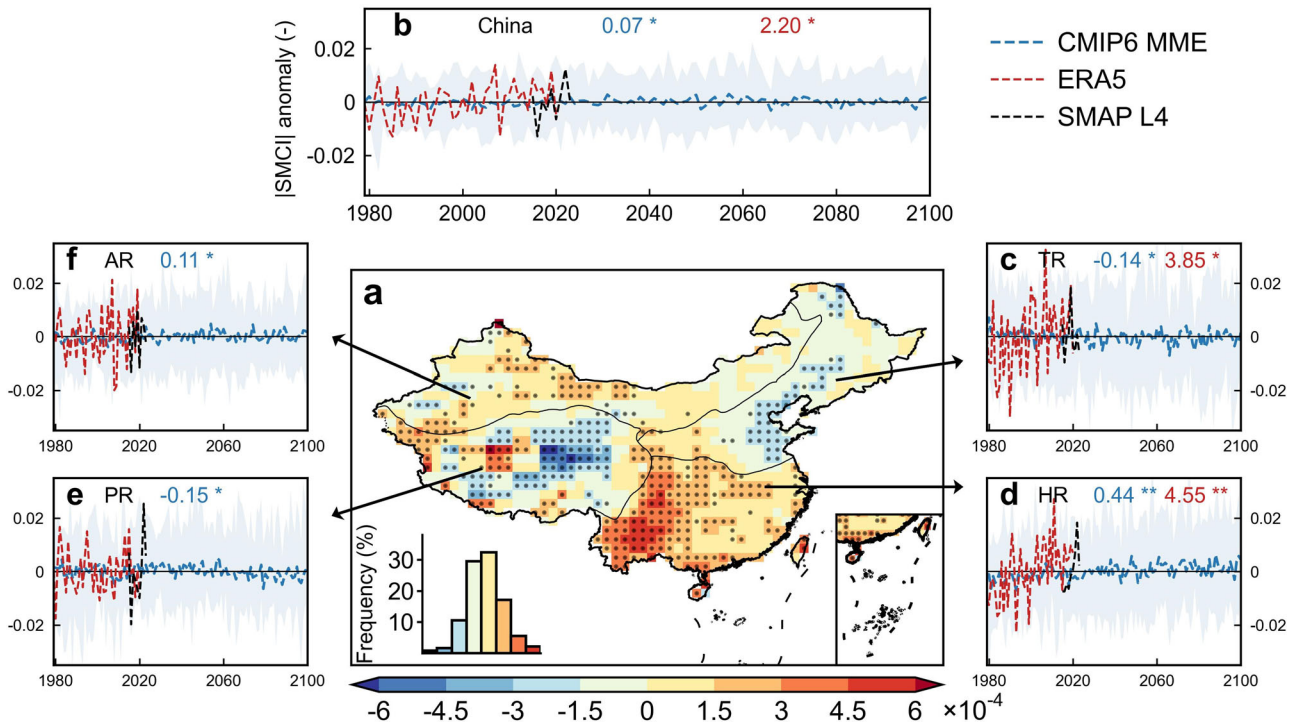
Fig. 2 | Temporal trends in the annual mean of |SMCI| for 1979–2100 estimated using the Theil–Sen estimator. a Spatial distribution of the temporal trend based on CMIP6 MME under the SSP2-4.5 scenario. The inset histogram at the bottom left displays the frequency of each level of temporal trend. Pixels with significant ($p < 0.05$) trend is highlighted by black dots. **b** Trends in the spatially averaged annual mean of |SMCI| anomaly based on CMIP6 MME, ERA5, and SMAP L4 over China. The blue shading envelope illustrates the spread of CMIP6 models under investigation, and the symbols of * and ** are annotated to indicate the regression significance level of $p < 0.05$ and $p < 0.01$, respectively. **c** the same as (**b**), but in TR, **d** HR, **e** PR, **f** AR.

Fig. 3 | Temporal trends of |SMCI| for 2015–2100 estimated using the Theil–Sen estimator. a Trends under the SSP2-4.5 scenario, **b** under the SSP5-8.5 scenario. Pixels with significant ($p < 0.05$) trend is highlighted by black dots. The inset histograms at the bottom left of each sub-figure display the frequency of each level of temporal trend.
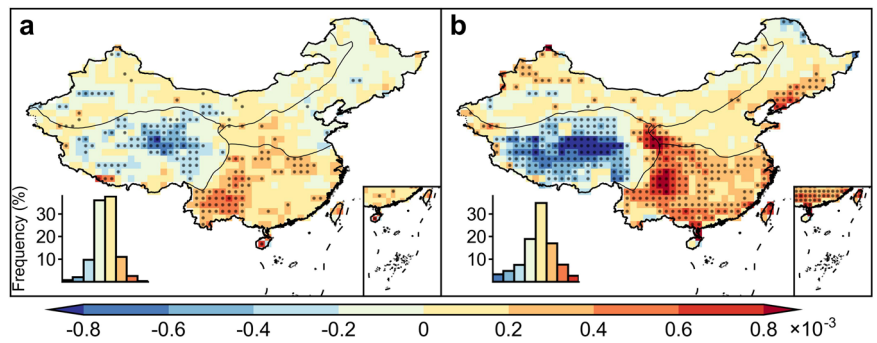
the DWAA event in this region, and this trend has already been frequently observed in Yunnan Province in the southwestern HR[33–35], where flash drought is commonly reported in the last four decades[34,36,37].

The annual anomaly of |SMCI| for China and each of the four subregions are shown in individual plots around the spatial map (Fig. 2). Across China, the CMIP6 MME projects |SMCI| to show a statistically significant ($p < 0.05$) increasing trend, indicating a trend of more concentrated SM in the coming decades. This is also evidenced by the ERA5 SM during 1979–2020. In contrast to the overall increasing trend of |SMCI|, PR shows a significant ($p < 0.05$) decreasing trend in |SMCI| from CMIP6, and this decreasing trend is projected to accelerate over the far future of this century (2070–2100). It is worth mentioning that the discrepancy in SMCI fluctuation between CMIP6 and ERA5 is likely due to the different vertical support[38] of these two SM datasets, as SM from CMIP6 and ERA5, respectively, represent simulations at a depth of ~10 and 7 cm, which may also explain the more consistent trend between ERA5 and SMAP L4 with vertical support of ~5 cm.

To illustrate the anthropogenic impact on the SMCI, we further compare |SMCI| changing trends under a median emission scenario (SSP2-4.5) and those under a high emission scenario (SSP5-8.5), which is a combined scenario of a high energy-intensive, socioeconomic developmental path with strong radiative forcing in Fig. 3.

Overall, under the SSP2-4.5 scenario, |SMCI| is projected to increase significantly in southwestern China, indicating a higher probability of DWAA in this area. This region has abundant water vapor sources from two channels: the Bay of Bengal and the South China Sea. Due to the abundance of water vapor, the equivalent potential temperature and atmospheric instability significantly increase under the warming climate[26], leading to more frequent short-duration intense precipitation[39]. Moreover, under the warming climate, the northwestward extension of the subtropical high pressure allows more warm and moist water vapor from the South China Sea to supplement this region, further promoting the increase in |SMCI| over this region[39].

Meanwhile, under the SSP5-8.5 scenario, much extensive areas along the coastal zone of southeastern China, northwestern China (or the western AR), and middle/lower reaches of the Yangtze River, are anticipated to be exposed to DWAA events. Overall, the paradigm of "wet season gets wetter, dry season gets drier (WWDD)"[21,40] is projected to be more prominent under a scenario with a greater increase in CO_2 emission and higher air temperature. Here, we define a pixel to be in alignment with the WWDD paradigm if there is a significant ($p < 0.05$) increase in its |SMCI| time series. About 9.5% of China conforms to the WWDD paradigm under SSP2-4.5, whereas this percentage increases to 24.3% under SSP5-8.5. One of the identified WWDD hot spots in our study is the southwest of HR, or southwestern China (Fig. 3), which coincides with region recognized as "wet get wetter" (WW) using satellite soil moisture dataset[41].

This discrepancy between median- and high-level emission scenarios is particularly prominent for HadGEM3-GC31-LL (Supplementary Fig. 4), whose percentage conforming to WWDD increases from 11.7 to 38.9%. In addition, GCMs with identical land surface models (LSM) show high consistency in WWDD paradigm identification, such as MIROC6 and MIROC-ES2L. GCMs with the latest version of LSM show higher agreement with MME in WWDD paradigm compared to those with obsolete LSM, as indicated by CMCC-ESM2 (with CLM4.5) versus NorESM2-MM (with CLM4), and ACCESS-CM2 (with CABLE2.5) versus ACCESS-ESM1-5 (with CABLE2.4).

The impacts on SMCI changing magnitude exerted by anthropogenic activities vary over different regions. Under the high emission scenario SSP5-8.5 over HR in central and southern China, the projected increase in |SMCI| and the consequent potential DWAA risk will be more prevailing compared to those under the SSP2-4.5 scenario (compare Fig. 3a, b). Similarly, the northeastern China and northern AR are projected to witness a greater and more significant increase in |SMCI|, and exhibit a higher risk of DWAA events. The unprecedented sudden shift between drought and flood has already been observed over AR in a more frequent manner[4], and is anticipated to boost in the future. In contrast, under the SSP5 scenario, PR is expected to experience a greater and more significant decrease in |SMCI|, showing more dispersed surface soil water resources.

The emerging hot spot analysis (EHSA) could identify hot (cold) spots that exhibit a statistically significant clustering of high (low) |SMCI| values, demonstrates similar patterns (Supplementary Fig. 5). First, the temporal concentration of surface soil water, expressed as |SMCI|, shows an overall opposing pattern to that of the spatial pattern of annual precipitation. This is consistent with the spatial pattern of SMCI shown in Fig. 1 (i.e., a |SMCI| hot spot prevails over AR while a |SMCI| cold spot prevails over HR, indicating the spatial clustering of high |SMCI| in AR and low |SMCI| in HR). Second, consistent with the Theil–Sen estimator, the intensity of spatial clustering of low |SMCI| over the eastern PR shows an overall increasing trend, and this increase is statistically significant ($p < 0.05$; shown as an intensifying cold spot). This indicates that SM is becoming more temporally dispersed in this region. In addition, the intensity of spatial clustering of low |SMCI| over the eastern HR shows an overall decreasing trend, significant at the $p < 0.05$ level (shown as a diminishing cold spot), indicating an increasing temporal concentration of SM, or movement towards the WWDD paradigm, in southern China. These trends are also magnified under the SSP5-8.5 scenario in EHSA.

Validation of our DWAA framework

The credibility of our proposed DWAA detection framework is validated against the records collected from statistical yearbooks and literature. Four prominent DWAA events are selected for such validation.

Event 1: DWAA in Yangtze River Basin (YRB) in 2011. According to the Bulletin of Flood and Drought Disaster in China (2011), DWAA events occurred in the middle/lower reaches of the YRB around June 3, 2011. In the same year, the China Meteorological Administration selected this event as one of the top ten extreme weather and climate events that received the most public attention domestically and abroad. Specifically,

from January to May 2011, over the YRB, the rainfall in Hubei (HB), Hunan (HN), Jiangxi (JX), Anhui (AH), and Jiangsu (JS) was 51.1% less than in the same period of past years, hitting a record low since 1951. In June of the same year, heavy rainfall occurred, causing an abrupt change from drought to flood in this region within a short time.

This spike of annual DW events in 2011 is well depicted by our DWAA framework, with 35.7% of YRB struck by DW at least once in 2011 according to ERA5 (hereinafter we refer "area fraction" as the fraction of certain areas that experienced at least one event within a certain period), and the number reached 7.3% for areas that encountered DW twice, exceeding its preceding and following years (Supplementary Fig. 6). In addition, the spatial pattern of the detected DWAA showed high frequency in the southwestern HB, and southern AH, well aligned with the bulletin record. In addition, around 20% of YRB consistently experienced DW events from 2010 to 2013, aligning with the DWAA hot spots identified by our framework in the following Section "Frequency of DWAA events".

Due to the intrinsic dynamic feature of SMCI, the DWAA event can be further broken down into daily scales (Fig. 4a). During 2011, the DWAA events over YRB peaked on June 3 and June 15, with DWAA area fractions of these two days (1.4 and 3.5%) far exceeded baseline, which highly aligned with the bulletin record.

Similar results of 2011 are observed in our DWAA framework using CMIP6 GCMs (Supplementary Fig. 7). Despite of discernable discrepancy between 20 selected CMIP6 GCMs, the CMIP6 MME showed high agreement with ERA5, with DW area fraction of YRB during 2011 attained 32.8%, and the number was 5.0% for areas that encountered DW twice. In addition, the DWAA detection results from CMIP6 MME are highly consistent with the ERA5 SM in terms of spatial distribution and area fraction. It should be noted that the configuration for the DWAA framework is set identical for both ERA5 and CMIP6. That is, both set the same half-window width ($T = 7$) for SMCI calculation, the same percentile for SMCI threshold (the 7th percentile for DW event) and SMA threshold (the 20th and 80th percentiles, respectively, for positive and negative values). This increases the fairness in the intercomparison of DWAA results using different SM datasets.

Event 2: DWAA in Yunnan Province in 2017. According to the China Meteorological Disasters Yearbook, from May to early ten days of June 2017, the whole of Yunnan Province witnessed a large negative precipitation anomaly percentage (PA) of lower than −50%, ranking the third lowest since 1961. On June 10, across Yunnan Province 83 stations recorded meteorological drought, 13 stations recorded severe drought, and 10 stations extreme drought. Over Yunnan Province, cities of Qujing (QJ), Lijiang (LJ) and Kunming (KM), and autonomous prefecture of Honghe (HH), all suffered from severe drought and adverse impact on agriculture. The abrupt shift from drought to flood or DW event occurred in the middle ten days of June, with heavy rainfall causing regional floods over central and eastern Yunnan Province.

This DW event can also be accurately identified in our DWAA framework (Fig. 4b and Supplementary Fig. 8). Spatially, HH, KM, QJ, and LJ in the mid-eastern of Yunnan Province are identified with extensive DW strikes. Temporally, on June 11 and 13, largest area of Yunnan Province experienced DW events (Fig. 4b). Our designed DWAA framework successfully detects the recorded DWAA event with more detailed spatial and temporal information.

Event 3: DWAA in Guangdong Province in 2015. According to the 86 metrological observations across Guangdong Province, from March to April 2015, the whole province witnessed a large negative PA, with the monthly PA in most cities and counties of the province lower than −50%. In May, the postponed yet more fierce flood season rapidly brought in abnormally high precipitation, especially in the northern Pearl River Delta and northern Guangdong, where the monthly PA reaches 100–160%[42]. In short, the unpunctual and unusual flood season induced this DW event in Guangdong Province in 2015.
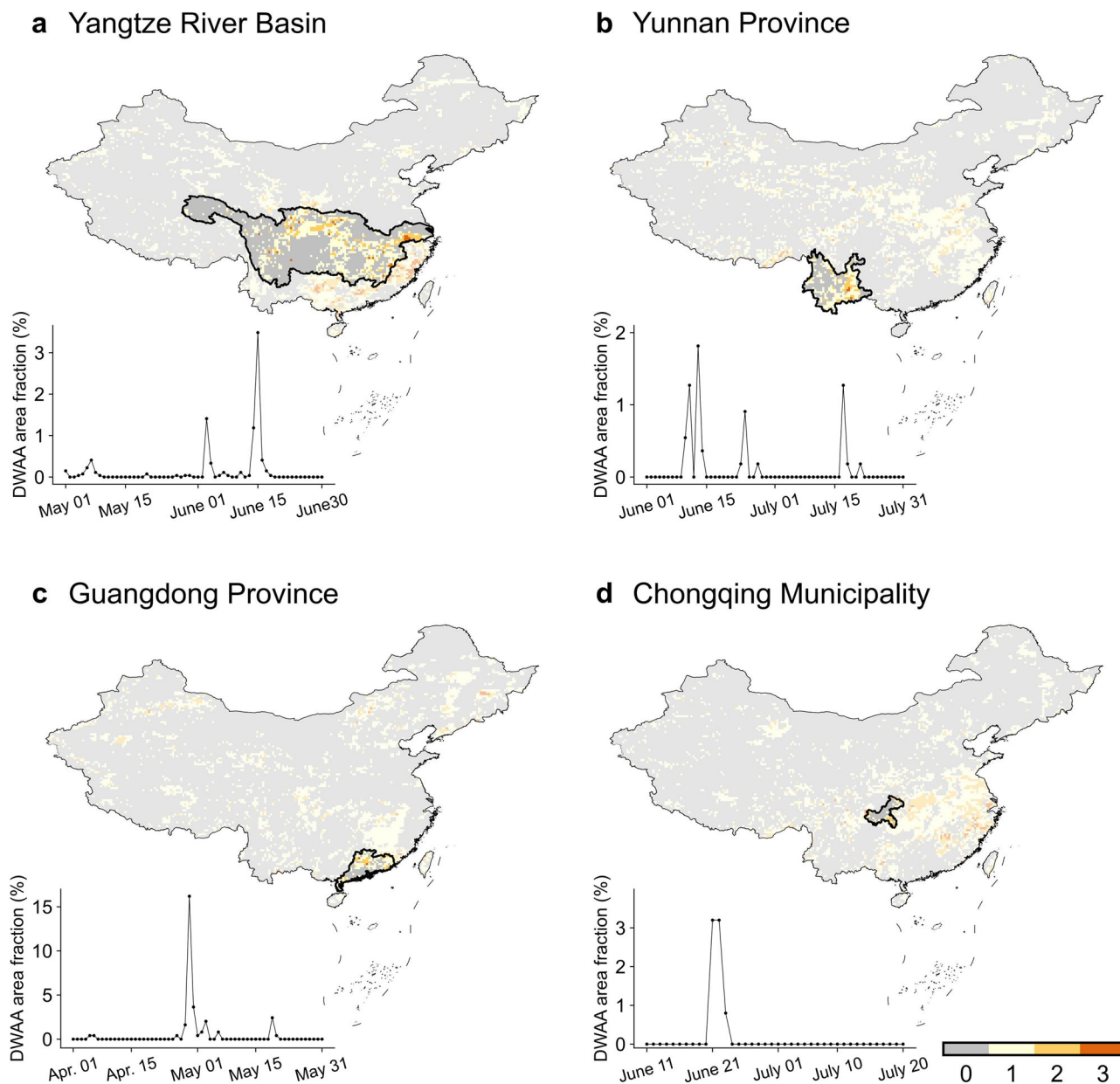
Fig. 4 | DW events identified in our DWAA framework using ERA5 daily SM. a YRB in 2011, **b** Yunnan Province in 2017, **c** Guangdong Province in 2015, and **d** Chongqing Municipality in 2000. The inset line charts at the bottom left of each sub-figure show the temporal evolution of the DWAA area fraction in the corresponding years.

This DW event can also be accurately identified from our DWAA framework (Fig. 4c and Supplementary Fig. 9). In terms of timing, the DWAA annual area fraction peaked in 2015, reaching almost 60%. Moreover, in terms of spatial distribution, the areas identified with more frequent DW events within Guangdong in 2015, such as the northern Pearl River Delta and northern Guangdong, coincided with areas recorded with prominent abrupt change from dry to wet status.

Event 4: DWAA in Chongqing Municipality in 2000. Based on precipitation of fixed months, Zhang et al. [43] employed summer long-cycle drought-flood abrupt alternation index and identified year 2000 with prominent DW event in Chongqing Municipality. This could be detected in our DWAA framework with more spatial details (Fig. 4d and Supplementary Fig. 10), clearly recognizing the northeast, southeast, and west of Chongqing with higher DW frequency.

The above-mentioned four DWAA events are all recorded and diagnosed based on meteorological observations of precipitation. This largely constrains our validation type to be DW event, which is largely determined

by precipitation. Even though, our DWAA framework provides more spatial and temporal details of the DWAA occurrences. On this basis, our DWAA framework fueled by CMIP6 SM is used to project the future DWAA events in China, and explore their spatiotemporal variation in the following section.

Frequency of DWAA events

Via the synergistic use of SMCI and SMA, DWAA events are identified using the framework proposed in Methods section. In Fig. 5a, b, we show the spatial distribution of the frequency of DW and WD events during 1979–2100 in China. For a fair comparison, the entire study period is divided into three sub-periods with equal length (S1: 1979–2019; S2: 2020–2060; and S3: 2061–2100). The frequencies of DW and WD events show similar spatial patterns among different sub-periods, while exhibiting high spatial heterogeneity among four different sub-regions. HR and coastal regions are more prone to DW events, while the junction of the HR and PR are more exposed to WD events.
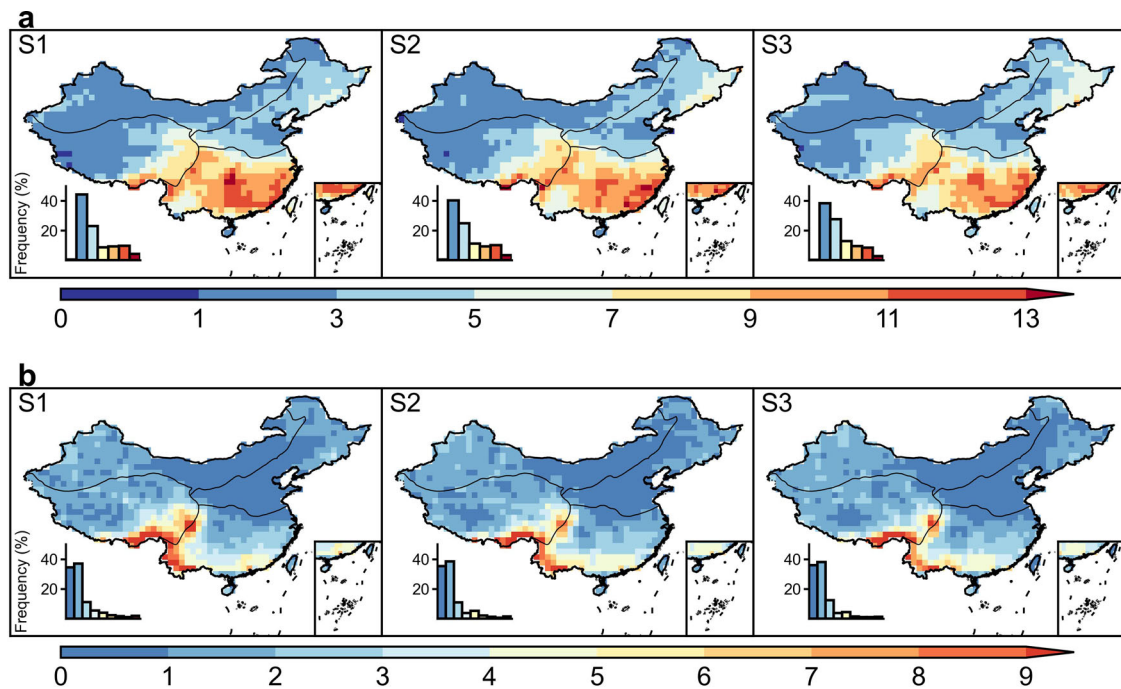
Fig. 5 | Frequency of DWAA events. Spatial distribution of **a** DW, **b** WD frequency in three sub-periods (S1: 1979–2019; S2: 2020–2060; and S3: 2061–2100) for CMIP6 MME under the SSP2-4.5 scenario.

The number of total occurrences count (hereinafter referred to as "occurrences") of DW and WD events are also compared between different emission scenarios of SSP2-4.5 and SSP5-8.5 (Fig. 6a). For a fair comparison, the occurrences here are spatially averaged to remove the impact of spatial extent. Overall, HR is projected to have the highest DWAA occurrences, while AR and TR are projected to experience the lowest DWAA occurrences. With increasing emission level, a notable increase is projected in WD occurrences, while the DW occurrences over entire China do not show significant increase. However, it should be noted that areas affected by DW are projected to increase across four sub-regions in different GCMs (Fig. 6b), while areas projected to be struck by WD is generally increasing except for PR, which aligns with the significant decrease in SMCI observed over PR with high emission level (Fig. 3). With increased emission level, more widespread area is affected by DWAA (Fig. 6b), and specifically, the increase in area fraction under the influence of DW event is slightly more prominent than that under the influence of WD event.

Inter-model differences are higher in WD occurrences projection than those in DW. In addition, GCMs with more advanced LSM show higher agreement with MME in DWAA prediction compared to those with obsolete LSM, as indicated by CMCC-ESM2 with CLM4.5 versus NorESM2-LM (NorESM2-MM) with CLM4.

From the perspective of intensity (Supplementary Fig. 11), HR is expecting the highest DW intensity, while southern PR and southwestern HR are expecting the highest WD intensity. Both are in alignment with their respective frequency patterns. This is corroborated by the recently more frequent record-breaking hydrological events, including the flash flooding in northwestern China[44–46], and flash drought in Yunnan Province[33–35].

Discussion

As shown in the temporal analysis of SMCI, both the Theil–Sen estimator and EHSA reveal that over southern China (or eastern HR), there is a significantly ($p < 0.05$) increasing trend in the temporal concentration of SM, or a movement towards the WWDD paradigm, especially under the SSP5-8.5 scenario. Precipitation, ET, and runoff could affect the changing pattern of the SMCI. Therefore, we examine the contribution from precipitation, ET, and runoff to SMCI using random forest (RF) regression analysis. Considering the availability of model simulations for the four pertinent variables

(SM, ET, runoff, and precipitation) under two scenarios in the future and during the historical period, only NorESM2-LM and NorESM2-MM meet this criterion. Therefore, we calculate the concentration indices for ET, runoff, and precipitation (denoted as ECI, RCI, and PCI, respectively), and further use the ECI, RCI, and PCI to predict SMCI via RF model. The method of calculating the ECI, RCI, and PCI is exactly the same as the method of calculating SMCI, just replacing the variable SM with the variable of interest. The prediction performance of the RF model is shown in Fig. 7a, while the variable with the highest importance for SMCI prediction is shown in Fig. 7b.

Variables control the variations of SMCI and DWAA frequency differ among four sub-regions. Over most of AR, ECI dominates SMCI fluctuations, which suggests that high ET driven by increasing temperature could be the main reason for the higher concentration in the temporal distribution of SM. In contrast, over the lower Yangtze River, which is highly affected by the western Pacific subtropical high (WPSH), the higher variability of precipitation denoted by PCI, is likely responsible for the SMCI pattern. The overall dominance patterns of ECI, RCI, and PCI over SMCI remain unchanged during the historical period 1979–2014 (Supplementary Fig. 12). The factors for characterizing the temporal dynamics of SM, and further SMCI, include properties such as terrain, soil texture, and vegetation. However, our major goal here is to analyze the relative importance of hydrological cycle components, so only the above three essential hydrological variables are considered in the RF model.

As the change in SMCI is largely attributable to the changing pattern of precipitation over HR and TR, it is therefore influenced by large-scale atmospheric circulation signaled by WPSH. The WPSH channels moisture from the tropics and underpins the East Asian summer climate. As a result, the interannual variability of the WPSH dominates climatic extremes in southern China[47,48]. In response to greenhouse warming, especially warm anomalies in the Indian and/or tropical Atlantic Ocean, an increase in future WPSH variability is projected by CMIP6, translating into an increased frequency of climatic extremes across the Chinese monsoon area[49–51], and increased temporal concentration of SM in the Yangtze River region.

In this study, a novel framework based on SMCI to detect the WWDD paradigm, and further investigate the DWAA frequency is proposed. This framework shows advantages in its usage of fine scale (daily to sub-daily) SM information for identifying the swift alternation of anomalous SM

Fig. 6 | DWAA occurrences and area fraction during 1979–2100 under the SSP2-4.5 and SSP5-8.5 scenarios. a Total occurrences of DWAA for four sub-regions of China normalized by spatial extent. Pixels that do not have a single DWAA are not considered. **b** Area fraction for four sub-regions of China that went through at least one DWAA event.
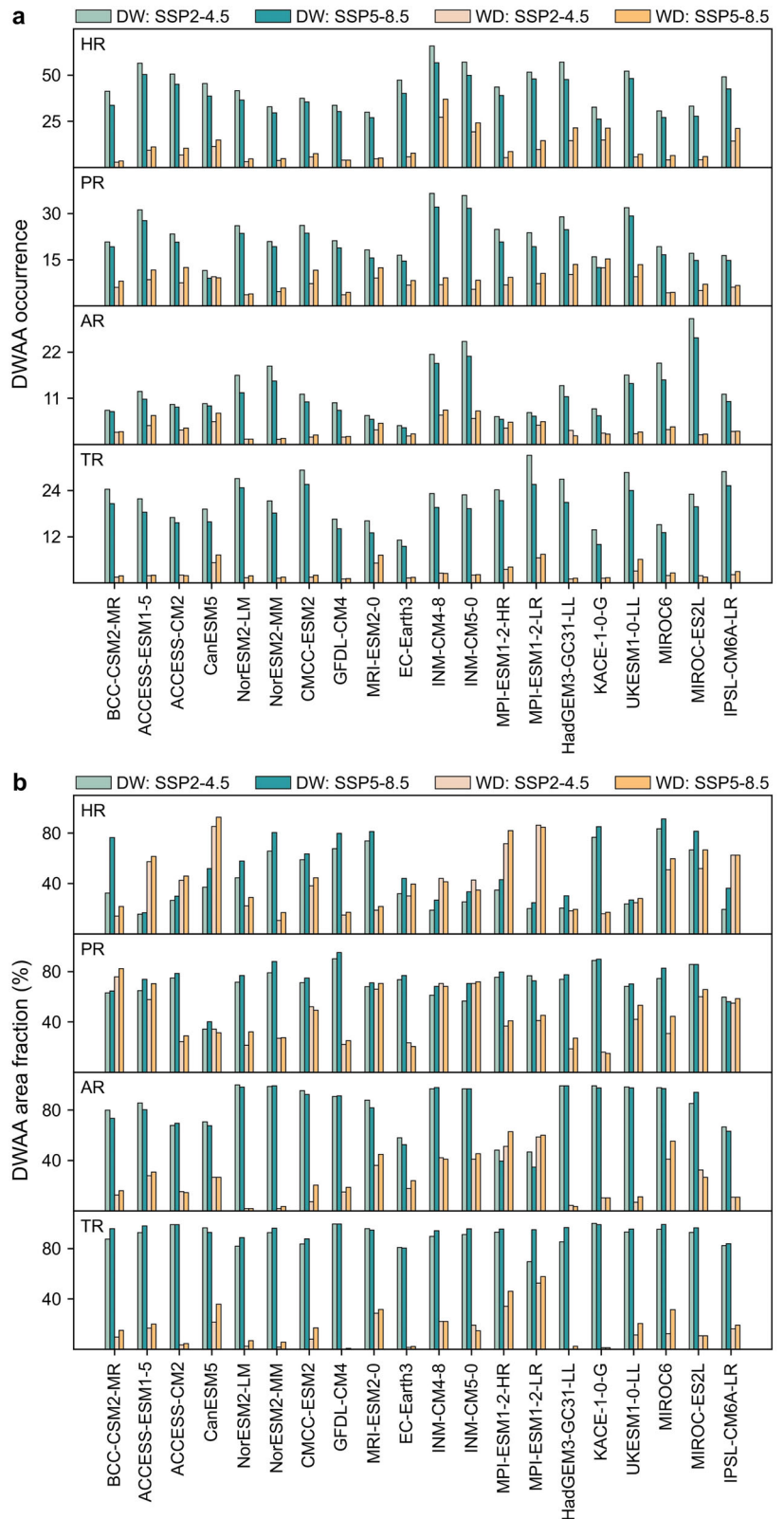
conditions, which is directly influential for terrestrial ecosystem. In addition, this framework is suitable for discerning both DW and WD events, which is superior to other univariate approaches.

We find that the SMCI over China generally shows consistent spatial patterns across different CMIP6 SM simulations, i.e., a higher SMCI over AR of northwestern China, and a lower SMCI over HR of southern China.

By the end of the 21st century, the SM over AR and HR is projected to be temporally more concentrated, conforming to the WWDD paradigm. Compared with the median emission level (SSP2-4.5 scenario), the higher emission (SSP5-8.5 scenario) enhances this concentration tendency, as the temporal concentration of SM increases more significantly over HR, while exhibiting an opposite trend over PR. All models consistently highlight the

Fig. 7 | Contributions of ECI, RCI, and PCI to SMCI variation for 2015–2100 under the SSP2-4.5 scenario. a RF model performance in Pearson correlation *R* between modeled and predicted SMCI, **b** feature with the highest importance in RF regression.
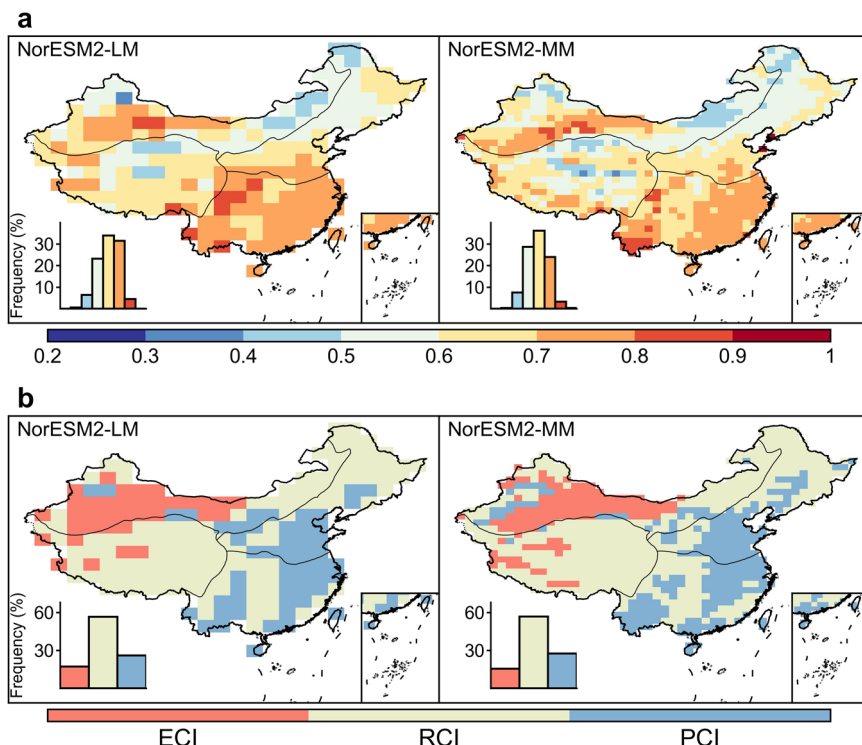

Table 1 | Datasets used in this study

Variable	Dataset	Temporal resolution	Spatial resolution (~lat × lon)	Time span
SM	CMIP6	daily	Cf. Table 2	1979–2100
	ERA5	hourly	0.25° × 0.25°	1979–2020
	SMAP L4	3-hourly	9km × 9km	2015–2023
Precipitation/ Runoff/ ET	NorESM2-LM	daily	1.875° × 2.5°	1979–2100
	NorESM2-MM	daily	0.94° × 1.25°	1979–2100

coastal zone of southeastern China as DW hot spot, and southwestern China as WD hot spot. Attribution analysis highlights the intensifying intra-annual variability in precipitation as the major reason for the observed increase in the SMCI over HR, where the WWDD paradigm is partly confirmed. Our work suggests that over the area highlighted as WWDD hot spot, efforts, including upgrading hydraulic engineering infrastructure, should be planned to tackle future DWAA.

Methods

Datasets

All datasets used in this study are listed in Table 1.

In this study, long-term SM information is obtained from GCMs within the CMIP6. GCMs include land surface processes to incorporate the climatic impacts on SM and the relative feedback of SM to the atmospheric forcing. Considering data availability, we use daily surface SM datasets from 20 CMIP6 models (Table 2), which include historical simulations (1979–2014) and future projections (2015–2100) under shared socioeconomic pathway 2 (SSP2-4.5) and 5 (SSP5-8.5). Specifically, SSP2-4.5 represents an additional radiative forcing of 4.5 W/m² in the year 2100 based on a medium forcing (or "business-as-usual") scenario, while SSP5-8.5 represents an additional 8.5 W/m² under a high forcing (high CO_2 emission) scenario[52,53]. Besides data availability, the 20 CMIP6 models are selected due to their relatively high performance in SM simulations according to validation results using the in-situ SM observation network[54,55]. To acquire multi-model ensemble mean, SM datasets from CMIP6 are resampled to 1° using nearest neighbor interpolation.

In addition to GCMs, we also include SM simulations from the fifth-generation reanalysis dataset ERA5 released by the European Centre for Medium-range Weather Forecasts[56]. The hourly SM data-sets from ERA5 during the period 1979–2020, with a spatial resolution of 0.25° × 0.25° and topsoil depth of 0–7 cm, are collected and aggregated into daily values.

Microwave-based SMAP L4 SM product[57,58], which assimilates SMAP brightness temperature observations into the catchment land surface model, is also used in this analysis. The 3-h surface SM (0–5 cm depth) dataset in SMAP L4 is selected and averaged to daily SM time series.

SMCI measuring the temporal concentration of SM time series

In this study, a novel SM-based index, namely SMCI, is proposed to measure the temporal concentration of SM time series within a time window of length L ($L = 2T + 1$ with T denoting the half-window length). The SMCI is a normalized measure in deviation degree of SM temporal distribution from the hypothetically uniform distribution, and can be calculated using the following steps (Fig. 8):

(i) Normalize the SM time series within a window of length L. To estimate the SMCI at time i, we first extract the SM time series θ_t centered at time i with half-window length of T: {θ_{i-T}, $\theta_{i-(T-1)}$, ..., θ_i, θ_{i+1}, ..., $\theta_{i+(T-1)}$, θ_{i+T}}, and then apply the min–max normalization to this SM time series.

$$\theta'_t = \frac{\theta_t - \theta_{\min}}{\theta_{\max} - \theta_{\min}} , \; i - T \leq t \leq i + T \qquad (1)$$

Table 2 | Details of the 20 selected GCMs in CMIP6

GCM	Land surface model	Spatial resolution (~lat × lon)	Member used
BCC-CSM2-MR	BCC_AVIM2	1.125° × 1.125°	r1i1p1f1
ACCESS-ESM1-5	CABLE2.4	1.25° × 1.875°	r1i1p1f1
ACCESS-CM2	CABLE2.5	1.25° × 1.875°	r1i1p1f1
CanESM5	CLASS3.6	2.8° × 2.8°	r1i1p1f1
NorESM2-LM	CLM4	1.875° × 2.5°	r1i1p1f1
NorESM2-MM	CLM4	0.94° × 1.25°	r1i1p1f1
CMCC-ESM2	CLM4.5	0.94° × 1.25°	r1i1p1f1
GFDL-CM4	GFDL-LM4.0.1	1.0° × 1.25°	r1i1p1f1
MRI-ESM2-0	HAL	1.125° × 1.125°	r1i1p1f1
EC-Earth3	HTESSEL	0.70° × 0.70°	r1i1p1f1
INM-CM4-8	INM-LND1	1.5° × 2.0°	r1i1p1f1
INM-CM5-0	INM-LND1	1.5° × 2.0°	r1i1p1f1
MPI-ESM1-2-HR	JSBACH	0.94° × 0.94°	r1i1p1f1
MPI-ESM1-2-LR	JSBACH	1.875° × 1.875°	r1i1p1f1
HadGEM3-GC31-LL	JULES	1.25° × 1.875°	r1i1p1f3
KACE-1-0-G	JULES	1.25° × 1.875°	r1i1p1f1
UKESM1-0-LL	JULES-ES-1.0	1.25° × 1.875°	r1i1p1f2
MIROC6	MATSIRO6.0	1.41° × 1.41°	r1i1p1f1
MIROC-ES2L	MATSIRO6.0	2.813° × 2.813°	r1i1p1f2
IPSL-CM6A-LR	ORCHIDEE 2.0	1.26° × 2.5°	r1i1p1f1

where, θ'_t is the normalized SM time series; θ_{max} (θ_{min}) is the maximum (minimum) of θ_t. In this paper, T is taken as 7 (unit: day) and the SMCI shows limited sensitivity to the parameter of T (Supplementary Fig. 13).

(ii) Estimate the accumulation of the normalized SM time series $f_1(t)$ within the same window (Fig. 8b, f). To facilitate the comparison of the accumulation curves, the accumulation of $f_1(t)$ is set to start from the coordinates of the origin, and the accumulation of the normalized SM sequence $\{0, \theta'_{i-T}, …, \theta'_i, …, \theta'_{i+T}\}$, or $f_1(t)$ is calculated as follows:

$$f_1(t) = \int_{i-T}^{i+T} \theta'_t dt \qquad (2)$$

(iii) Estimate the accumulation of hypothetically uniformly-distributed SM $f_2(t)$ within the same window (Fig. 8c). It is estimated by assuming that the total amount of surface soil water content within the window is distributed in a temporally uniform manner. Similar to (ii), the accumulation of $f_2(t)$ starts from the coordinates of the origin.

$$\bar{\theta'_t} = \frac{\int_{i-T}^{i+T} \theta'_t dt}{2T+1} \qquad (3)$$

$$f_2(t) = \int_{i-T}^{i+T} \bar{\theta'_t} dt \qquad (4)$$

(iv) Normalize the difference between $f_1(t)$ and $f_2(t)$ (Fig. 8d, g). The integrals of the difference between $f_1(t)$ and $f_2(t)$ within the same window of $[i - T, i + T]$ is computed, and divided by the integral of $f_2(t)$ to obtain the SMCI estimates at time i. Similar to (ii) and (iii), the accumulation of

numerator and denominator both start from the coordinates of the origin.

$$SMCI = \frac{\int_{i-T}^{i+T} [f_1(t) - f_2(t)] dt}{\int_{i-T}^{i+T} f_2(t) dt} \qquad (5)$$

It should be noted that the SMCI is sign-sensitive, or we can differentiate between the WD and DW event by comparing whether the slope of the accumulative curve of the normalized SM time series is larger than the slope of the uniformly-distributed time series. For instance, if $f_1(t)$ curve is concave, or the SMCI is negative (Fig. 8a–d, and the first sub-graph of the "Example of DW event" in Fig. 9, where SMCI <0). In this case, SM is first drier than the hypothetically uniform distribution and then wetter than the uniform distribution baseline, suggesting a higher potential of experiencing a DW event. In contrast, a case where the SMCI is positive suggests a higher risk of a WD event (Fig. 8e–g, and the first sub-graph of the "Example of WD event" in Fig. 9, where SMCI >0). Unlike the conventional PCI, this two-sided feature of the SMCI matches the two-sided spectrum of DWAA events, and thus meets the requirement to investigate both DW and WD types of abrupt alternation events. The above-mentioned procedure is illustrated in the column "Step1: Calcuate SMCI" of Fig. 9.

DWAA event detection

As mentioned above, the SMCI reflects the degree of deviation of SM from a uniform distribution within a given time window. When the SMCI approximates zero, this indicates that SM is evenly distributed over time, and there is a low likelihood of a DWAA event. In contrast, when the |SMCI| largely deviates from zero, a more concentrated SM distribution is expected, and there is a higher probability of a DWAA event. Therefore, we first select a SMCI threshold for identifying possible DWAA events.

We sort all positive SMCI estimates from 122 years (1979–2100) of CMIP6 simulations in ascending order per pixel, and take the SMCI corresponding to the 70th percentile as the threshold (Th_{pos}) for detecting potential WD event. Likewise, we take the SMCI corresponding to the 7th percentile of all negative SMCI values as the threshold (Th_{neg}) for detecting potential DW events. Note that the 70th and 7th percentiles are determined iteratively by sensitivity analysis (Supplementary Fig. 14). All local maximum and minimum SMCIs exceeding Th_{pos} and Th_{neg} are regarded as potential DWAA occurrences, and the corresponding time (P) is recorded. Owing to the large variation in soil texture and differences in local hydroclimatic properties over the study area, we take individual thresholds for each pixel to accurately detect DWAA events ("Step 2: Select possible events" in Fig. 9).

It should be noted that only using the local extreme of SMCI for DWAA detection could lead to false alarms. For instance, in a case with an anomalously wet SM state, if intensive precipitation continues, there are a correspondingly rapid increase in the SM, resulting in a localized maximum SMCI, which could be mistakenly identified as a DWAA event. Therefore, we also incorporate information on the SMA to enhance the accuracy of DWAA event detection.

SMA is estimated by subtracting the SM raw value at time i from the multi-year mean SM ($\overline{SM}$) at time i across the study period and divided by $\overline{SM}$ as follows:

$$SMA = \frac{SM - \overline{SM}}{\overline{SM}} \times 100\% \qquad (6)$$

The SMA is classified into dry and wet states using the threshold A_{neg} and A_{pos}: (i) classified as dry state when SMA < A_{neg}; (ii) classified as wet state when SMA > A_{pos}. The A_{neg} (A_{pos}) is determined by sorting all negative (positive) SMA values in ascending order and taken at the 80th (20th) percentiles.

With the ancillary information of SMA, this framework is capable of discerning whether the actual alternation from an anomalously wet to
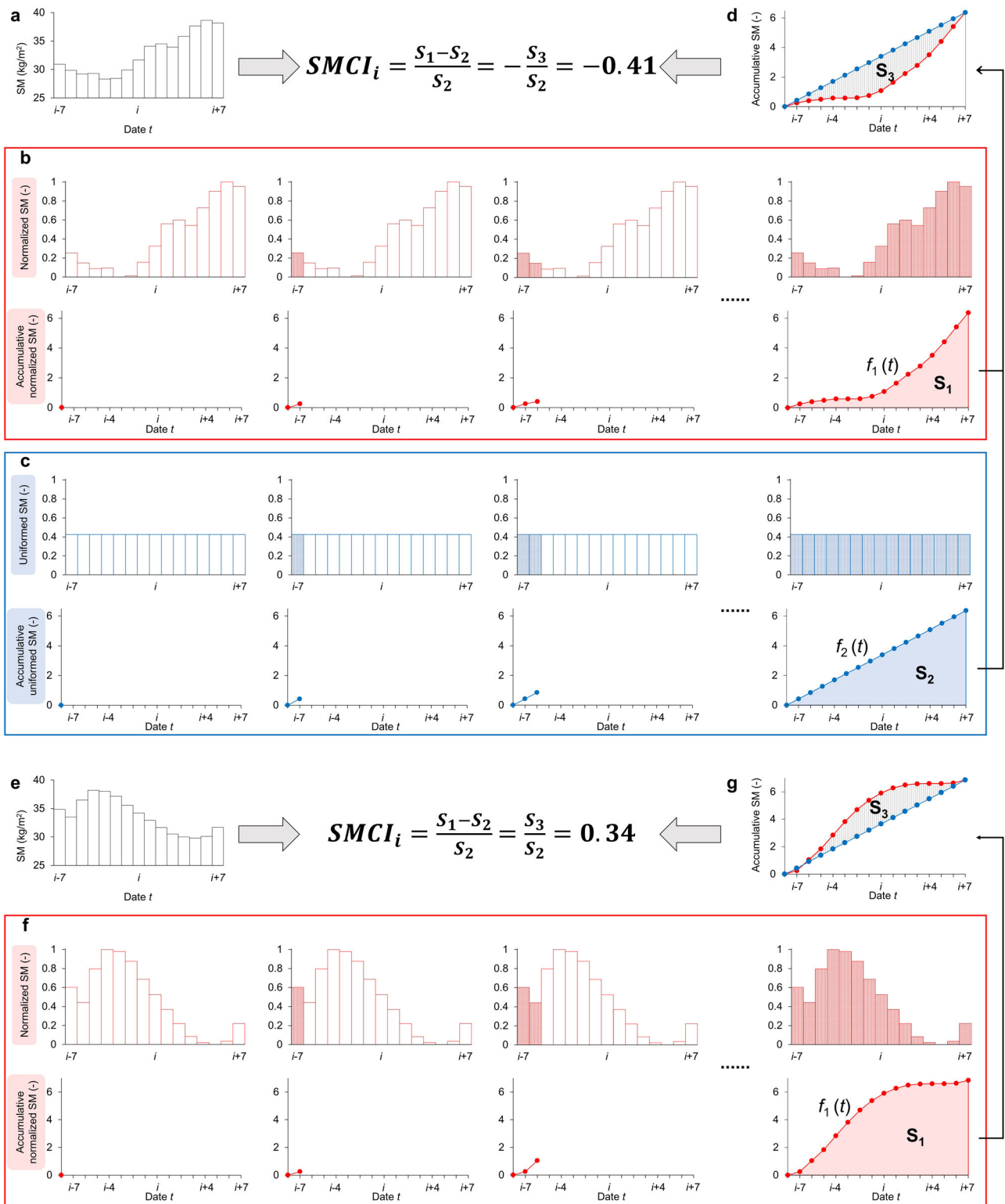
Fig. 8 | Detailed calculation process of SMCI. a Raw SM time series as an illustrative example which generates negative SMCI, **b** calculation process of the accumulation of the normalized SM time series, **c** calculation process of the accumulation of the hypothetically uniformly-distributed SM time series, **d** calculation result of SMCI; **e–g** the same as (**a, b, d**), respectively, but as an example which generates positive SMCI.

anomalously dry state (or vice versa) occurs at the potential DWAA time point P. Specifically, we can safely identify P as an incidence of DW if all the following conditions are satisfied: the SMA shows (i) an anomalously dry state for more than D_1 days (prior period), (ii) an anomalously wet state for more than D_2 days (post period), and (iii) the alternation (transition period C) completes within less than 5 days. This procedure is illustrated in "Step 3:

Identify DWAA" in Fig. 9. A similar procedure can be used to identify incidences of WD. The synergistic use of SMCI and SMA can correctly identify a continuously anomalous dry status before and after a potential alternation P_1, and thus avoid the false detection of DWAA events at P_1, meanwhile successfully identifies a "true" DW event at P_2 (row labeled "Example of DW event" in Fig. 9). Similarly, the incorrect identification of
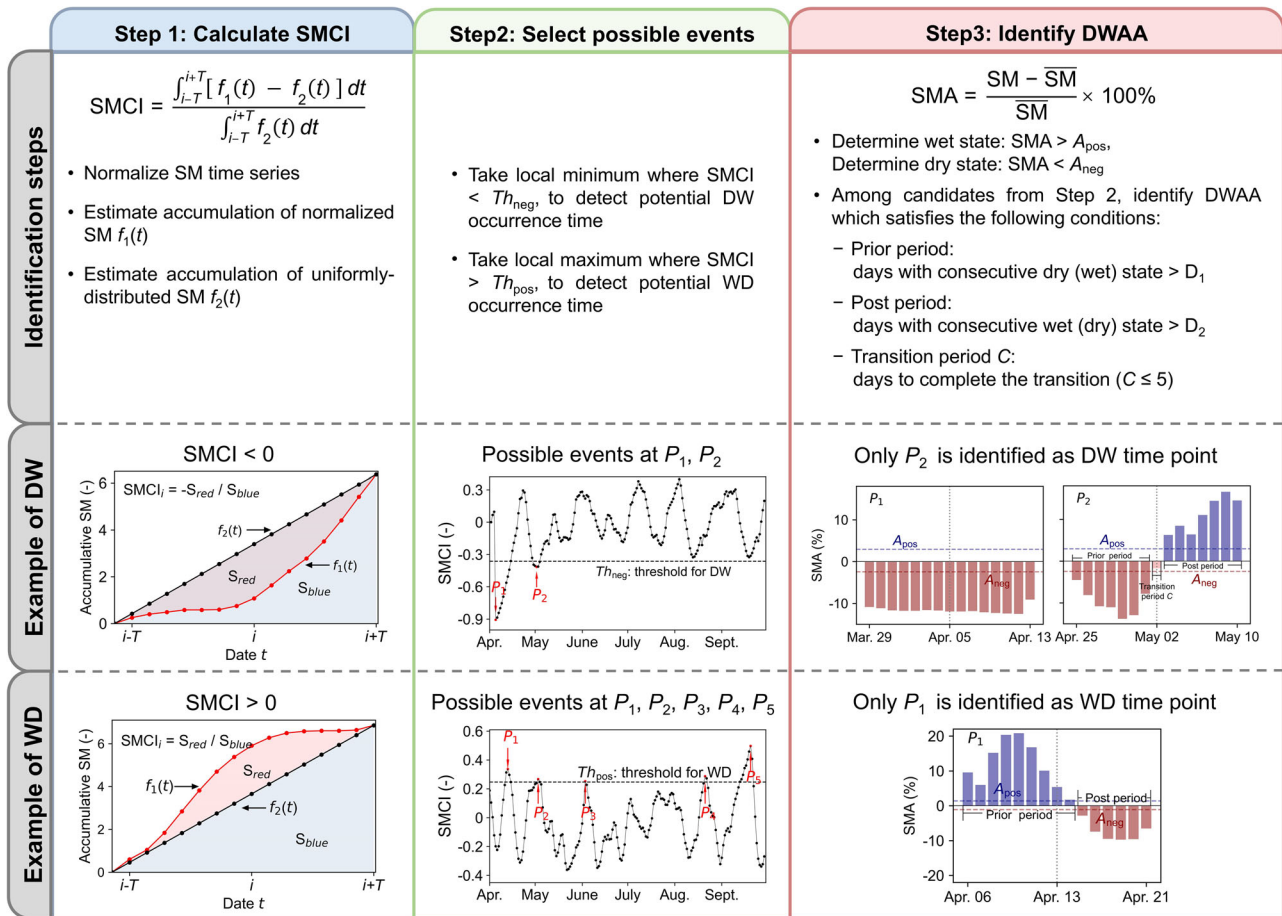
Fig. 9 | Illustration of DWAA detection framework. The first row introduces the identification steps for DWAA events, and the second and third rows explain in detail the identification processes for a DW and WD event respectively.

the P_2, P_3, P_4 and P_5 is avoided, and the WD event at P_1 is correctly identified in the row labeled "Example of WD event" in Fig. 9.

The intensity of a DWAA event is estimated by the SMA maximum and minimum during the event and the number of days C to complete the transition as follows:

$$Intensity = \frac{SMA_{max} - SMA_{min}}{C} \qquad (7)$$

Theil–Sen analysis and Mann–Kendall test

Trends are first calculated using Theil–Sen analysis[59,60], and then the Mann–Kendall (MK) test[61,62] is used to determine the significance of each trend. Theil–Sen analysis is also known as Sen's slope estimation, a robust nonparametric statistical approach to estimate the temporal trend of time series, calculated as follows:

$$\beta = Median\left[\frac{x_j - x_k}{j - k}\right] \qquad (8)$$

where β is the estimated magnitude of the trend in the time series, and x_j and x_k are time series j and k ($j > k$) with length n, respectively.

The MK test is a nonparametric time series trend test that does not require data to obey a normal distribution, and is unaffected by missing values and outliers. The statistic S, is calculated as:

$$S = \sum_{k=1}^{n-1} \sum_{j=k+1}^{n} sgn\left(x_j - x_k\right) \qquad (9)$$

The trend test is performed using the test statistic z, which is calculated as follows:

$$z = \begin{cases} \frac{S-1}{\sqrt{Var(S)}} & (S > 0) \\ 0 & (S = 0) \\ \frac{S+1}{\sqrt{Var(S)}} & (S < 0) \end{cases} \qquad (10)$$

$$Var(S) = \frac{n(n-1)(2n+5)}{18} \qquad (11)$$

Using a two-sided test, the null hypothesis of no trend is rejected if $|z| > z_{(1 - p/2)}$ at a given significance level p. $z_{(1 - p/2)}$ refers to the z-score for which the cumulative probability is equal to 1 - $p/2$ in the standard normal distribution.

Emerging hot spot analysis (EHSA)

EHSA[63,64] is also used to extract the spatiotemporal pattern of the SMCI. A hot spot is defined as a location that exhibits statistically significant clustering (strong local autocorrelation) within a spatial pattern. Regions in the non-random set of high and low values of the feature of interest (namely SMCI) are identified using the Getis-Ord Gi* statistic[65], which returns the z-score of SMCI for each location with an associated p-value (statistical probability); the MK method is then used to identify hot and cold spot trends (Supplementary Table 1).

Random forest (RF) regression

We use the RF regression algorithm to establish relationships between SMCI and relevant hydrometeorological variables in the surface water cycle. The

RF regression is a machine learning algorithm based on classification trees[66]. RF uses a bootstrap resampling method to draw multiple samples from the original sample, model the decision tree for each bootstrap sample, and then combine the predictions of multiple decision trees to arrive at the final prediction by voting. The merits of RF model include (i) efficient handling of high-dimensional datasets and non-requirement of feature selection as the feature subset is chosen randomly; (ii) readily measurement of the relative importance of each feature on the estimates, which makes it highly suitable for attribution analysis. Therefore, based on RF analysis, key control factors determining the SMCI spatial pattern are evaluated.

Data availability

The ensembles of Coupled Model Intercomparison Project Phase 6 (CMIP6) simulations are available at https://aims2.llnl.gov/search/cmip6/. The ERA5 hourly volumetric soil water data are available at https://cds.climate.copernicus.eu/. The SMAP L4 3-hourly 9 km EASE-Grid surface and root zone soil moisture data (V007) are available at https://nsidc.org/data/smap. The data used to create the figures can be found at https://doi.org/10.6084/m9.figshare.25295566.

Code availability

Codes used to generate main figures are available on request from the corresponding author.

References

1. Christian, J. I. et al. Global distribution, trends, and drivers of flash drought occurrence. *Nat. Commun.* **12**, 1–11 (2021).
2. IPCC. *Climate Change 2021: The Physical Science Basis* (2021).
3. Meza, I. et al. Global-scale drought risk assessment for agricultural systems. *Nat. Hazards Earth Syst. Sci.* **20**, 695–712 (2020).
4. Bi, W. et al. Drought-flood abrupt alteration events over China. *Sci. Total Environ.* **875**, 162529 (2023).
5. Hao, Z. & Singh, V. P. Compound events under global warming: a dependence perspective. *J. Hydrol. Eng.* **25**, 03120001 (2020).
6. Zhu, R. et al. Cumulative effects of drought–flood abrupt alternation on the photosynthetic characteristics of rice. *Environ. Exp. Bot.* **169**, 103901 (2020).
7. Ren, J. et al. Evolution and prediction of drought-flood abrupt alternation events in Huang-Huai-Hai River Basin. *China Sci. Total Environ.* **869**, 161707 (2023).
8. Shi, W. et al. Drought-flood abrupt alternation dynamics and their potential driving forces in a changing environment. *J. Hydrol.* **597**, 126179 (2021).
9. Bordoloi, S., Ni, J. & Ng, C. W. W. Soil desiccation cracking and its characterization in vegetated soil: a perspective review. *Sci. Total Environ.* **729**, 138760 (2020).
10. Zeng, H. et al. Drought-induced soil desiccation cracking behavior with consideration of basal friction and layer thickness. *Water Resour. Res.* **56**, e2019WR026948 (2020).
11. Bi, W. et al. Evolution of drought–flood abrupt alternation and its impacts on surface water quality from 2020 to 2050 in the Luanhe River Basin. *Int. J. Environ. Res. Public. Health* **16**, 691 (2019).
12. Ren, Y. et al. Earlier spring greening in Northern Hemisphere terrestrial biomes enhanced net ecosystem productivity in summer. *Commun. Earth Environ.* **5**, 122 (2024).
13. Huang, S., Hou, B., Chang, J., Huang, Q. & Chen, Y. Copulas-based probabilistic characterization of the combination of dry and wet conditions in the Guanzhong Plain. *China J. Hydrol.* **519**, 3204–3213 (2014).
14. Luo, Y. et al. Safety design for water-carrying Lake flood control based on copula function: a Case study of the Hongze Lake, China. *J. Hydrol.* **597**, 126188 (2021).
15. Wu, Z., Li, J., He, J. & Jiang, Z. Large-scale atmospheric singularities and summer long-cycle droughts-floods abrupt alternation in the middle and lower reaches of the Yangtze River. *Chin. Sci. Bull.* **51**, 2027–2034 (2006).
16. Gu, L., Chen, J., Yin, J., Xu, C.-Y. & Zhou, J. Responses of precipitation and runoff to climate warming and implications for future drought changes in China. *Earths Future* **8**, e2020EF001718 (2020).
17. Wan, W., Zhao, J., Popat, E., Herbert, C. & Döll, P. Analyzing the impact of streamflow drought on hydroelectricity production: a global-scale study. *Water Resour. Res.* **57**, e2020WR028087 (2021).
18. Vicente-Serrano, S. M., Beguería, S. & López-Moreno, J. I. A multiscalar drought index sensitive to global warming: the standardized precipitation evapotranspiration index. *J. Clim.* **23**, 1696–1718 (2010).
19. Palmer, W. C. *Meteorological Drought* (U.S. Department of Commerce, Weather Bureau, 1965).
20. Byrne, M. P. & O'Gorman, P. A. The response of precipitation minus evapotranspiration to climate warming: Why the "wet-get-wetter, dry-get-drier" scaling does not hold over land. *J. Clim.* **28**, 8078–8092 (2015).
21. Greve, P. et al. Global assessment of trends in wetting and drying over land. *Nat. Geosci.* **7**, 716–721 (2014).
22. Greve, P. & Seneviratne, S. I. Assessment of future changes in water availability and aridity. *Geophys. Res. Lett.* **42**, 5493–5499 (2015).
23. Feng, S. et al. Improved estimation of vegetation water content and its impact on L-band soil moisture retrieval over cropland. *J. Hydrol.* **617**, 129015 (2023).
24. Wheeler, D., Shaw, G. & Barr, S. *Statistical Techniques in Geographical Analysis* (Routledge, 2004).
25. Martin-Vide, J. Spatial distribution of a daily precipitation concentration index in peninsular Spain. *Int. J. Climatol.* **24**, 959–971 (2004).
26. Long, K. et al. Higher temperature enhances spatiotemporal concentration of rainfall. *J. Hydrometeorol.* **22**, 3159–3169 (2021).
27. Mood, A. M. The distribution theory of runs. *Ann. Math. Stat.* **11**, 367–392 (1940).
28. Chen, H. & Sun, J. Changes in drought characteristics over China using the standardized precipitation evapotranspiration index. *J. Clim.* **28**, 5430–5447 (2015).
29. Piao, S. et al. The impacts of climate change on water resources and agriculture in China. *Nature* **467**, 43–51 (2010).
30. Xu, F. et al. Understanding climate change impacts on drought in China over the 21st century: a multi-model assessment from CMIP6. *Npj Clim. Atmos. Sci.* **7**, 1–12 (2024).
31. Oliver, J. E. Monthly precipitation distribution: a comparative index. *Prof. Geogr.* **32**, 300–309 (1980).
32. Huang, J. et al. Global climate impacts of land-surface and atmospheric processes over the Tibetan Plateau. *Rev. Geophys.* **61**, e2022RG000771 (2023).
33. Zhao, D., Deng, S. & Zhang, J. Spatiotemporal characteristics of dry-wet abrupt alternation events in China during 1960–2018. *Int. J. Climatol.* **42**, 9612–9625 (2022).
34. Zhang, S. et al. The intensification of flash droughts across China from 1981 to 2021. *Clim. Dyn.* **62**, 1233–1247 (2024).
35. Fu, K. & Wang, K. Quantifying flash droughts over China from 1980 to 2017. *J. Geophys. Res. Atmos.* **127**, e2022JD037152 (2022).
36. Zhu, Y. et al. Causes of the severe drought in Southwest China during the summer of 2022. *Atmos. Res.* **303**, 107320 (2024).
37. Gong, Z. et al. The features of regional flash droughts in four typical areas over China and the possible mechanisms. *Sci. Total Environ.* **827**, 154217 (2022).
38. Schmidt, T. et al. Comprehensive quality assessment of satellite- and model-based soil moisture products against the COSMOS network in Germany. *Remote Sens. Environ.* **301**, 113930 (2024).

39. Jiang, R., Cui, X., Lin, J. & Tian, J. 40-Year statistics of warm-season extreme hourly precipitation over Southwest China. *J. Appl. Meteorol. Climatol.* **62**, 1891–1908 (2023).

40. Xiong, J., Guo, S., Abhishek, Chen, J. & Yin, J. Global evaluation of the "dry gets drier, and wet gets wetter" paradigm from a terrestrial water storage change perspective. *Hydrol. Earth Syst. Sci.* **26**, 6457–6476 (2022).

41. Peng, C. et al. Global spatiotemporal trend of satellite-based soil moisture and its influencing factors in the early 21st century. *Remote Sens. Environ.* **291**, 113569 (2023).

42. Yu, L., Mai, J., Ji, Z. & Zhang, D. Analysis of the abrupt alternation from drought to flood around the onset of rainy season in Guangdong in 2015. *J. Trop. Meteorol.* **37**, 611–622 (2021).

43. Zhang, T., Tang, H., Lei, T., Xiang, B. & Li, Y. The relationship between summer drought – flood abrupt alternation in Chongqing and the anomalous of atmospheric circulation. *J. Yunnan Univ.* **36**, 79–87 (2014).

44. Wang, N. et al. Spatiotemporal clustering of flash floods in a changing climate (China, 1950–2015). *Nat. Hazards Earth Syst. Sci.* **21**, 2109–2124 (2021).

45. Yin, J. et al. Flash floods: why are more of them devastating the world's driest regions? *Nature* **615**, 212–215 (2023).

46. Zhang, J. et al. Transforming flash floods into resources in arid China. *Land Use Policy* **76**, 746–753 (2018).

47. Wang, B., Xiang, B. & Lee, J.-Y. Subtropical high predictability establishes a promising way for monsoon and tropical storm predictions. *Proc. Natl Acad. Sci. USA* **110**, 2718–2722 (2013).

48. Ding, Y. & Chan, J. C. L. The East Asian summer monsoon: an overview. *Meteorol. Atmos. Phys.* **89**, 117–142 (2005).

49. Huang, Z., Zhang, W., Geng, X. & Jin, F.-F. Recent shift in the state of the western Pacific subtropical high due to ENSO change. *J. Clim.* **33**, 229–241 (2020).

50. Xu, H. et al. Juxtaposition of western Pacific subtropical high on Asian Summer Monsoon shapes subtropical East Asian precipitation. *Geophys. Res. Lett.* **47**, e2019GL084705 (2020).

51. Yang, K. et al. Increased variability of the western Pacific subtropical high under greenhouse warming. *Proc. Natl Acad. Sci. USA* **119**, e2120335119 (2022).

52. O'Neill, B. C. et al. The scenario model intercomparison project (ScenarioMIP) for CMIP6. *Geosci. Model Dev.* **9**, 3461–3482 (2016).

53. Riahi, K. et al. The shared socioeconomic pathways and their energy, land use, and greenhouse gas emissions implications: an overview. *Glob. Environ. Change* **42**, 153–168 (2017).

54. Fan, K., Zhang, Q., Li, J., Chen, D. & Xu, C.-Y. The scenario-based variations and causes of future surface soil moisture across China in the twenty-first century. *Environ. Res. Lett.* **16**, 034061 (2021).

55. Wang, A., Kong, X., Chen, Y. & Ma, X. Evaluation of soil moisture in CMIP6 multimodel simulations over conterminous China. *J. Geophys. Res. Atmos.* **127**, e2022JD037072 (2022).

56. Hersbach, H. et al. The ERA5 global reanalysis. *Q. J. R. Meteorol. Soc.* **146**, 1999–2049 (2020).

57. Entekhabi, D. et al. The soil moisture active passive (SMAP) mission. *Proc. IEEE* **98**, 704–716 (2010).

58. Piepmeier, J. R. et al. SMAP L-band microwave radiometer: instrument design and first year on orbit. *IEEE Trans. Geosci. Remote Sens.* **55**, 1954–1966 (2017).

59. Şen, Z. Innovative trend analysis methodology. *J. Hydrol. Eng.* **17**, 1042–1046 (2012).

60. Şen, Z. Trend identification simulation and application. *J. Hydrol. Eng.* **19**, 635–642 (2014).

61. Mann, H. B. Nonparametric tests against trend. *Econometrica* **13**, 245 (1945).

62. Kendall, M. G. *Rank Correlation Methods* (Griffin, 1948).

63. Ahmadi, H., Argany, M., Ghanbari, A. & Ahmadi, M. Visualized spatiotemporal data mining in investigation of Urmia Lake drought effects on increasing of PM10 in Tabriz using Space-Time Cube (2004-2019). *Sustain. Cities Soc.* **76**, 103399 (2022).

64. Deng, X., Gao, F., Liao, S., Liu, Y. & Chen, W. Spatiotemporal evolution patterns of urban heat island and its relationship with urbanization in Guangdong-Hong Kong-Macao greater bay area of China from 2000 to 2020. *Ecol. Indic.* **146**, 109817 (2023).

65. Getis, A. & Ord, J. K. The analysis of spatial association by use of distance statistics. *Geogr. Anal.* **24**, 189–206 (1992).

66. Breiman, L. Random forests. *Mach. Learn.* **45**, 5–32 (2001).

Acknowledgements

Author contributions
J.Q. and C.H. conceived the research, performed the analysis, and wrote the manuscript. J.Q., C.H., X.L., L.G., C.T., X.W., D.K., J.-P.W., D.C., and J.X. assisted in the interpretation of the results and revision of the manuscript.

Competing interests
The authors declare no competing interests.

Additional information
Supplementary information The online version contains supplementary material available at https://doi.org/10.1038/s41612-024-00808-w.

Correspondence and requests for materials should be addressed to Jianxiu Qiu.

Reprints and permissions information is available at http://www.nature.com/reprints

Publisher's note Springer Nature remains neutral with regard to jurisdictional claims in published maps and institutional affiliations.